

# Micromachined Fabry–Pérot Interferometer with Embedded Nanochannels for Nanoscale Fluid Dynamics

Koen M. van Delft, Jan C. T. Eijkel,\* Dragana Mijatovic, Tamara S. Druzhinina, Helmut Rathgen, Niels R. Tas, Albert van den Berg, and Frieder Mugele

MESA<sup>+</sup> Institute for Nanotechnology, University of Twente, P.O. Box 217, 7500 AE Enschede, The Netherlands

Received October 18, 2006; Revised Manuscript Received December 7, 2006

## ABSTRACT

We describe a microfabricated Fabry–Pérot interferometer with nanochannels of various heights between 6 and 20 nm embedded in its cavity. By multiple beam interferometry, the device enables the study of liquid behavior in the nanochannels without using fluorescent substances. During filling studies of ethanol and water, an intriguing filling mode for partially wetting water was observed, tentatively attributed to the entrapment of a large amount of gas inside the channels.

Research into the properties of fluids at the nanoscale historically has been the domain of physical chemists (colloid chemistry) and physicists (fluid mechanics and friction). First versions of the surface forces apparatus for the study of liquid properties on the nanoscale were thus built in the 1950s and 1960s by colloid chemists Derjaguin, Sparnaay, and Overbeek.<sup>1</sup> This device was further developed in a successful manner by the physicists Tabor, Winterton, and Israelachvili in the early 1970s.<sup>2,3</sup> Versions of it are still employed today,<sup>4,5</sup> but the field of nanofluidics has since greatly expanded thanks to the arrival of new detection and manipulation methods such as atomic force microscopy and the advent of micro- and nanotechnology to produce nanoscale structures and in particular nanochannels.<sup>6</sup>

Upon decreasing the channel height, a serious detection problem arises. Optical microscopy is by far the most frequently used method, however, when nanochannels become thinner than approximately 20 nm, direct optical discrimination between gas- and liquid-filled areas becomes very difficult due to the small differences in optical path length. Often, recourse is then taken to fluorescent solutes, however, both spatial and temporal information from these markers do not necessarily reflect the dynamics of the fluid. Adsorption to the channel walls, charge exclusion, dielectric effects, and pH variations can all alter the fluorescence intensity with photobleaching posing an additional problem.

In the surface forces apparatus, the optical thickness  $d_{\text{opt}} = d \cdot n$  ( $d$ : geometric thickness;  $n$ : refractive index) of confined liquid films is routinely measured with a resolution of approximately 0.1 nm using multiple beam (or “Fabry–Pérot”) interferometry. For this purpose, thin layers of silver are deposited on the back sides of micrometer thick atomically smooth mica sheets between which the thin liquid films of interest are placed. In the present manuscript, we demonstrate a design of a micromachined nanochannel device into which we integrate the multiple beam interferometry principle by embedding silver mirrors at micrometer distance into the channel walls. We present preliminary experiments of capillarity driven filling of channels with a height between 6 and 20 nm without taking recourse to fluorescent solutes. In this manner, the successful detection technology of the SFA is combined with the easy connectivity and experimental flexibility gained by the use of nanochannels.

Owing to their relatively simple configuration, Fabry–Pérot interferometers are the most frequently used spectrometers in microtechnology. The main design challenges for both static etalon and moveable mirror designs are to achieve parallelism between the two mirrors and to fabricate mirrors with sufficient reflectivity and low roughness.<sup>7</sup> Several movable interferometers were reported using a microelectrostatic actuated membrane fabricated out of silicon, silicon nitride, or several dielectric layers (Bragg mirror) with adjustable displacements ranging from 70 nm up to 1  $\mu\text{m}$ . Applications of micromachined interferometers include mo-

\* Corresponding author. E-mail: j.c.t.eijkel@utwente.nl. Address: BIOS/Lab-on-a-Chip Group, University of Twente, P.O. Box 217, 7500 AE Enschede, The Netherlands. Telephone: 053-4892839.

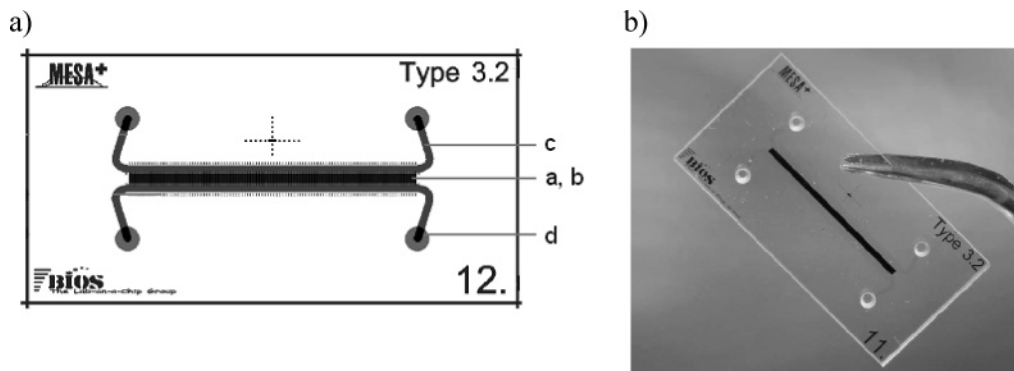


**Figure 1.** Nanofluidic chip design. (a) Chip layout with 3 and 10  $\mu\text{m}$  wide nanochannels with a length of 0.5 mm covered by silver mirrors (a,b), microchannels (c), and connection holes for fluid supply (d). (b) Photograph of the device; the 100 parallel nanochannels are located below the black line (formed by the silver mirror)

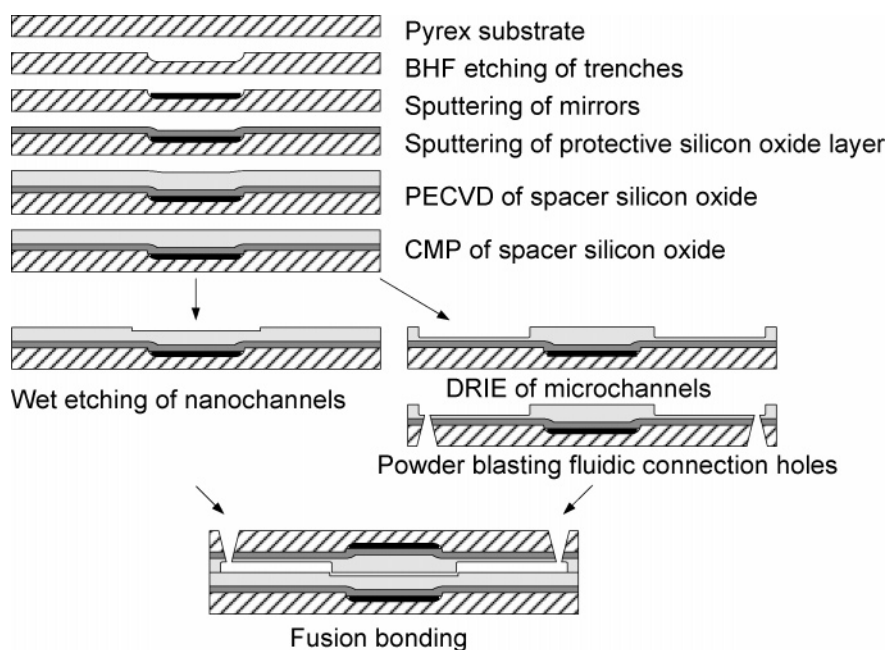


**Figure 2.** Schematic overview of the fabrication process (see text).

tion detectors, gas sensors, optical detectors for biological fluids,<sup>8–13</sup> and interferometers in combination with atomic force microscopes (AFM) for data storage and retrieval.<sup>14</sup> Furthermore, micromachined Fabry–Pérot interferometers with movable mirrors have also been used as tunable laser cavities.<sup>15</sup>

Nanochannels have been fabricated by a variety of methods and in various materials, resulting in channels of sub-100 nm scale in one or two dimensions.<sup>16</sup> The smallest 1-D nanochannels produced in Pyrex at present are to our knowledge the channels of Mao and Han with a height of 25 nm.<sup>17</sup> Smaller 1-D channels (down to 5 nm height) have been produced in silicon/glass.<sup>18</sup> The devices presented here incorporate the smallest up-to-date 1-D glass/glass nanochannels. Several groups have reported capillary filling experiments in micromachined nanochannels down to 27 nm height.<sup>19,20</sup> Drying experiments on nanochannels showed very rapid drying rates ascribed to corner flow.<sup>21</sup>

The manufacturing of devices was done in the MESA<sup>+</sup> cleanroom. The chip layout is shown in Figure 1a. The 10

mm  $\times$  20 mm chip has four fluidic connection holes (d) toward two parallel microchannels, which connect to 100 parallel nanochannels in between. The nanochannels are 500  $\mu\text{m}$  long, either 3 or 10  $\mu\text{m}$  wide, and 6, 11, 16, and 20 nm high. Both below and above the nanochannel section, silver mirrors with a thickness of 45 nm were embedded into the substrates. The mirrors are separated from the nanochannels by an approximately 1.1  $\mu\text{m}$  thick spacer layer of plasma-enhanced chemical vapor deposited (PECVD) silicon oxide.

Figure 2 shows a schematic overview of the fabrication process. After cleaning and dehydrating the Pyrex substrates, trenches were patterned using standard photolithography and etching in a buffered hydrogen fluoride (BHF) solution. Subsequently, an about 1 nm thick adhesion layer of Ta, 45 nm of Ag, and again 1 nm of Ta adhesion layer were deposited in the trenches. Redundant mirror material was removed in a lift-off process. Then an approximately 30 nm thick layer of silicon oxide was sputtered at 400  $^{\circ}\text{C}$  on the entire wafer, protecting the silver from tarnishing during further processing. Next, an approximately 1.1  $\mu\text{m}$  spacer

layer of silicon oxide was deposited by PECVD. To remove the steps caused by the lowering of the mirrors into the substrate earlier in the process, chemical mechanical polishing (CMP) was employed, removing approximately 75 nm of silicon oxide.

In the top wafer, channels of approximately 900 nm deep were etched using standard lithography and reactive ion etching (RIE). Subsequently, fluidic connection holes were fabricated using lithography and high-precision powder blasting. Nanochannels were etched into the bottom wafer using conventional lithography and wet etching in a 0.5% HF solution. Prior to bonding, channel depths and roughness were measured by AFM. The wafer pair was cleaned and bonded by means of fusion bonding and annealed at the relatively low temperature of 400 °C for 1 h to prevent destruction of the silver mirrors caused by the high mobility of the silver. Despite the low annealing temperature, the bond strength proved to be sufficient during the experiments. Finally, the wafer pair was diced. A fabricated chip is shown in Figure 1b.

The experimental setup consisted of a stabilized optical bench on which the components were mounted. White light from a Xe lamp was passed through a motorized grating monochromator. The bandwidth of the exiting light could be adjusted between 0.28 and 10 nm around the center wavelength by choosing between various exit slits. The monochromatic light was parallelized and used to illuminate the chip, which was mounted on an inverted microscope. The transmitted light was collected with the microscope objective and recorded with a 12 bit digital CCD camera. Both the camera and the monochromator were connected to a computer on which were custom-written Labview and Matlab programs for control and image recording.

For device characterization, chips were mounted in a custom-made chip holder. From the top part, fused-silica capillaries (internal diameter 101  $\mu\text{m}$ ) were connected using Nanoport connectors and ferrules (Upchurch Scientific). Transmission spectra were recorded typically in a range from  $\lambda = 400$  to 600 nm in steps of 0.1 nm. Figure 3 shows the transmitted intensity (laterally averaged over a small area of approximately  $5 \times 5 \mu\text{m}^2$ ) as a function of the incident wavelength for two neighboring locations, one on top of a nanochannel and the other one next to it. From the width and the separation of the transmission peak, the effective finesse was calculated to judge the quality of the interferometer. The ratio between the free spectral range and the full width at half-maximum at the wavelength of 506.4 nm was determined to be 26.6. Correcting for a mirror roughness (root-mean-square) of 1 nm, the theoretical finesse of the perfect system would be 27.4. Obviously, the mirror roughness has only a minor influence on the quality of the optical system. The reflectance of the mirrors was calculated to be 0.89. Only two of the three peaks in the wavelength range displayed in Figure 3 are affected by the presence of the nanochannel, namely those that correspond to standing waves inside the interferometer that have an antinode in the middle of the spacer layer where the channel is located. Due to the small thickness of the nanochannels, it can be shown that

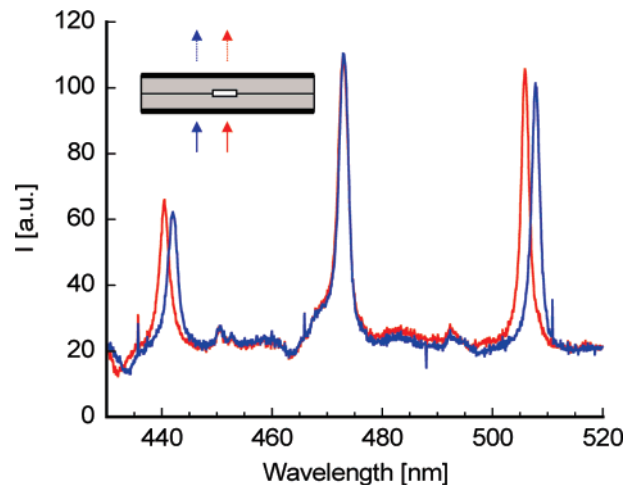


**Figure 3.** Transmission spectra on top (red) and next to (blue) a nanochannel (see inset). From the observed peak shift, the height of the nanochannel can be calculated. Only every other peak is shifted because of the symmetry in the optical system. The inset also indicates the elements in of the optical model: Ag mirrors (thick black lines), spacer layers (gray), nanochannel (white).

**Table 1.** Channel Heights Obtained with the FSC Method and AFM.

no.	FSC $\pm$ S.D. [nm]	AFM ( $\pm 10\%$ ) [nm]
1	$6.8 \pm 2.2$	$6.4 \pm 0.2$
3	$12.9 \pm 2.6$	$12.3 \pm 0.6$
2	$17.1 \pm 1.7$	$16.2 \pm 1.0$
4	23.0	$20.7 \pm 0.3$

the shift of these “sensitive” peaks is proportional to the difference in optical path length with respect to the surrounding spacer medium, i.e., for rigid channels, the peak shift is a direct measure of the refractive index of the medium inside the channel.

The height of the nanochannels was determined from the transmission spectra by numerically fitting calculated transmission spectra for the optical multilayer system, as sketched in the inset of Figure 3 to the measured spectra. The transmission was calculated using the standard matrix method for dielectric multilayers.<sup>22</sup> Using the independently determined dispersion relations of the materials involved, the transmission spectra are functions of the thicknesses of the SiO<sub>2</sub> spacer layers, the protective cover layers, and the nanochannel. To reduce the computational effort the so-called fast spectral correlation (FSC) method<sup>23</sup> was used. All optical characterization procedures follow the procedures described in detail in ref 24.

From the spectrum next to the channel in Figure 3, a spacer layer thickness of 2.1317  $\mu\text{m}$  was obtained. Using this value, the fitting procedure was repeated for a spectrum on top of an air-filled nanochannel with the channel height as fit parameter. This entire procedure was performed at a number of locations on the channels and averaged. The results are shown in Table 1 and compared to the depth of the trenches measured ex situ by AFM prior to bonding. The average height and standard deviation for the AFM measurements were calculated from five measurements on a 30  $\mu\text{m}$  long

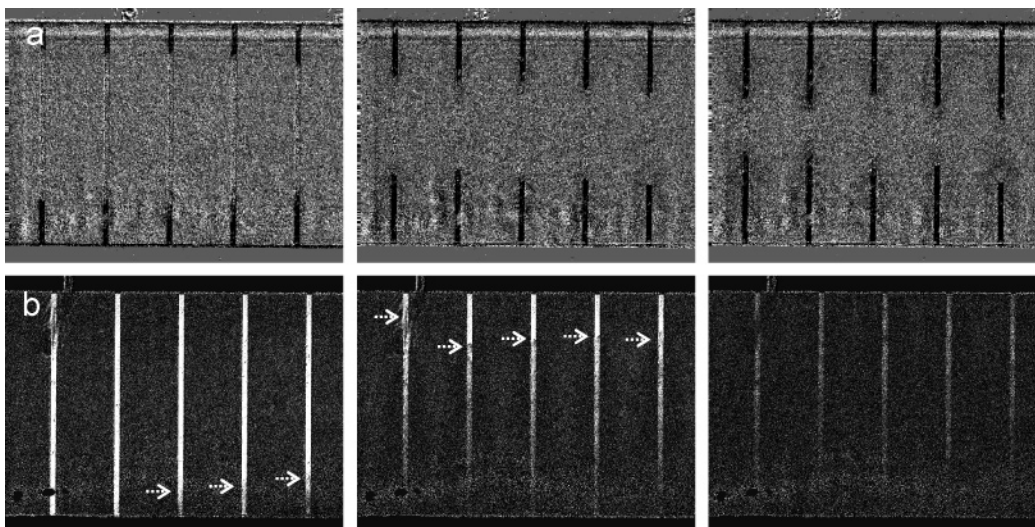


**Figure 4.** Video snapshots during channel filling (channel width:  $10\ \mu\text{m}$ ). Time between images: 0.5s. (a) Ethanol penetrating 6 nm channel simultaneously from both sides. (b) water filling an 12 nm channel. The arrows in (b) indicate the positions of the menisci where appropriate. Note the intensity gradient in the filled channel behind the meniscus in (b) (see text for details). The vertical lines are channels with filled channels appearing darker.

channel section. While the data for both methods are consistent within the error margins, the optical results seem to be systematically higher. This may be due to an additional spacing introduced by the finite width of the bonding plane between the two spacer layers, or to the offset ( $\pm 10\%$ ) of the AFM. The large standard deviation in the optical measurements partially reflects the roughness of the channel walls, which can lead to variations of the channel height by as much as  $\approx 2\ \text{nm}$  over lateral scales of a few tens of micrometers. Another source of uncertainty is the optical dispersion of the mirror and spacer materials, which depends strongly on details of the manufacturing process. From the AFM data, we find a small-scale roughness of 0.7 nm rms in agreement with previous measurements.<sup>25</sup>

The visualization of channel filling proceeded as follows. Upon filling with a liquid, the sensitive peak wavelengths of the transmission spectrum shift toward the wavelengths obtained next to the channel (see Figure 3) because the optical contrast decreases as the refractive index of the material inside the channel increases. For the typical design parameters described above, this wavelength shift is approximately 0.25 nm per nm change in optical thickness of the channel. In a procedure earlier applied to the surface forces apparatus, the device was illuminated with monochromatic light of a wavelength on one of the wings of a sensitive transmission peak (see Figure 3), typically the peak slightly above 500 nm. Under typical conditions, the transmitted intensity thereby was proportional to the average refractive index of the medium inside the channel within the range of interest. By taking images of the device in transmission, the evolution of refractive index profiles inside the channel could be directly followed at high image acquisition rates.

The capillary filling dynamics of channels of 6, 12, and 16 nm height were recorded in high-resolution videos, using a  $100\times$  magnification objective and a frame rate of 20 frames per s. The bandwidth of the incident light was 4.3 nm

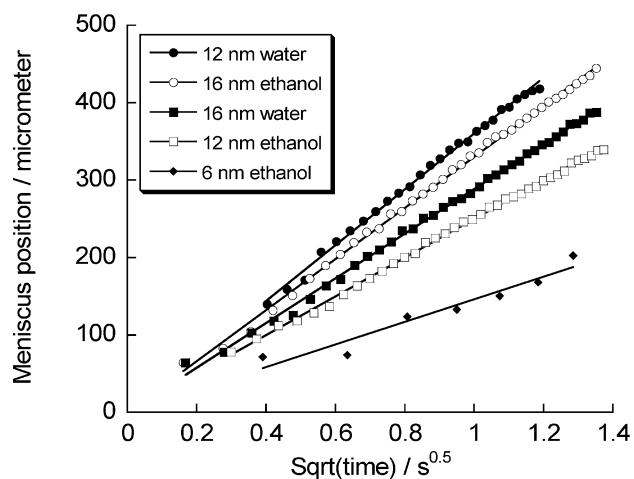


**Figure 5.** Meniscus position vs  $\sqrt{t}$ .

(fwhm). Ethanol or water was injected into the microchannels using a motorized syringe pump. Figure 4 shows a series of images recorded during spontaneous filling of a 6 nm channel with ethanol (a) and a 12 nm channel with water (b). In the first example, ethanol was admitted to the nanochannels from both sides, in the second one only from one side. The meniscus position could be followed easily in both cases. Interestingly, the right panel in (b), in which all menisci have reached the top end of the channels, displays an intensity gradient along the channel, which we will come back to in more detail below. Figure 5 shows that the menisci advance proportional to the square root of time. This plot is motivated by the classical Lucas–Washburn law of capillarity-driven channel filling:<sup>26</sup> a constant driving force  $f_{\text{cap}} = 2\sigma_{\text{lv}} \cos \theta$  per unit length (across the channel) pulls the liquid into the channel. Under quasistatic conditions, this force was balanced by the hydrodynamic resistance of the liquid between the moving meniscus and the entrance of the channel. The latter is given by  $f_{\text{visc}} = 2\mu x v'(0) = ((12\mu x)/d) \dot{x}$  for standard Poiseuille flow, where  $x$  and  $\dot{x}$  are the position and the

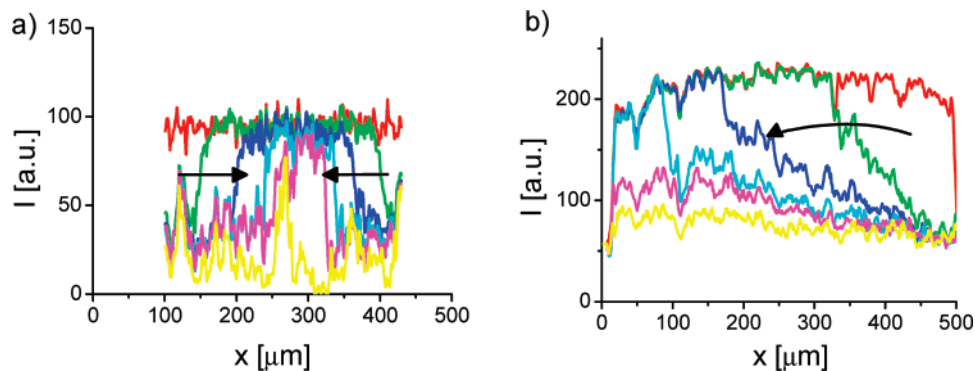


**Figure 6.** Transmitted intensity along channel every 0.5 s. The empty channels correspond to the constant high transmission levels, the filled ones to the lower ones. Arrows indicate the evolution with time: (a) 6 nm channel filled with ethanol simultaneously from both sides, (b) 12 nm channel filled with water from the right.

**Table 2.** Measured and Calculated Slopes of the Ethanol Filling Curves<sup>a</sup>

channel height/nm	$a_m$ [ $\mu\text{m s}^{-0.5}$ ]	$a_c$ [ $\mu\text{m s}^{-0.5}$ ]	C
16.2 nm (EtOH)	330	363	1.21
12.3 nm (EtOH)	250	317	1.61
6.4 nm (EtOH)	146	228	2.43
16.2 nm (H <sub>2</sub> O)	288	188	0.42
12.3 nm (H <sub>2</sub> O)	360	164	0.21

<sup>a</sup> C is the ratio  $a_c/a_m$ .

speed of the meniscus and  $v'(0)$  is the gradient of the flow profile at the solid–liquid interface. Equating these two force contributions and integrating the resulting differential equation yields the Lukas–Washburn solution

$$x(t) = \sqrt{\frac{\sigma_{lv} \cos \theta d}{3\mu}} \cdot \sqrt{t} \equiv a_c \sqrt{t} \quad (1)$$

Obviously, the meniscus dynamics obeys the expected  $\sqrt{t}$  dependence. However, the coefficients deviate from the macroscopic expectations, as shown in Table 2. Interestingly, we found two different types of behaviors: for ethanol, the measured coefficient is smaller than expected, while for water, the opposite was found. (For the comparison, we used macroscopic contact angles of  $0^\circ$  (ethanol) and  $29^\circ$  (water) measured on planar surfaces that were subject to the same preparation procedure as the channels.) While a reduced filling speed was found previously by others and was attributed to various effects such as electroviscosity, increased fluid viscosity, a channel deformation due to capillary-induced negative pressure,<sup>27</sup> and an increasing influence of the channel roughness,<sup>28,29</sup> we are not aware of previous reports of enhanced filling speeds.

While a detailed analysis of the above observations goes beyond the scope of the present publication, the superior resolution of the interferometric technique gives hints to the possible explanations compared to previous measurements. Figure 6 shows representative intensity cross sections (averaged over the channel width) as a function of time. The plot reveals a characteristic difference between the filling dynamics of ethanol and water in these experiments. In the case of ethanol, there is a well-defined intensity level for both the

empty channel and the filled channel. When the meniscus passes, the intensity level drops instantaneous to the lower filled level. In the 12 nm water channel, there is also a sharp intensity decrease at the meniscus; however, the decrease only amounted to approximately half of the transition from the empty-to-full channel. A linear intensity gradient develops behind the moving meniscus, which vanishes only on a rather slow time scale of the order 1 s. Interestingly, the same phenomenon is much less pronounced for the 16 nm channel (not shown).

This observation means that the optical thickness of the channel just behind the meniscus is dropping by less than 50% of the expected amount. Possible explanations for such a behavior can be: (i) the channel is fully filled but elastically deformed due to the high negative pressure behind the moving meniscus or (ii) the channel is initially only partial filling with liquid, e.g., due to entrapment of substantial amounts of nanoscale air bubbles. A simple energy balance between the meniscus force and the elastic energy yields indeed a channel height variation  $\Delta h \approx w\sigma_{lv}/(hE) = O(1 \text{ nm})$  that would be consistent with the observation. The linear pressure variation between the moving meniscus and the channel entrance could then explain the linear intensity variation. On the other hand, the existence and unusual stability of nanobubbles have attracted a lot of attention recently because of their enormous impact on the viscous drag between fluids and solid walls.<sup>30</sup> Owing to the free-slip boundary condition at liquid–gas interfaces in contrast to the classical hydrodynamic no-slip boundary at solid–liquid interfaces, the presence of gas bubbles reduces the viscous drag dramatically. This could explain the enhanced filling speed of water in our experiments, although the low macroscopic contact angle seems to disfavor their existence. While we are currently unable to identify the correct scenario, it is clear that small air bubbles are present on somewhat larger scales, as shown in Figure 7. The entrapment of these bubbles is promoted by the finite roughness of the channel walls: the meniscus does sometimes not move as a straight front across the channel but rather meanders, running ahead either along the edges of the channel (“corner flow”) or along other regions of locally reduced height within the channel.

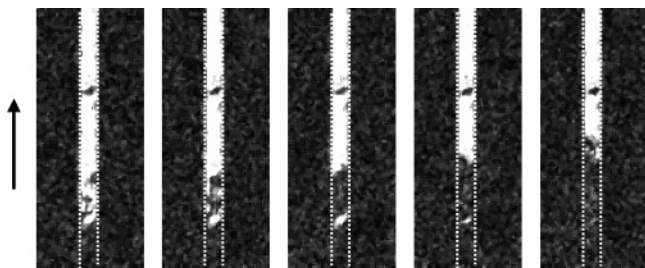


**Figure 7.** Close-up of an ethanol meniscus (dark) filling a 12 nm channel (width: 10  $\mu\text{m}$ ) from bottom to top. Note the meandering motion, which leads to the entrapment and subsequent dissolution of a gas bubble. Dotted lines indicate the positions of the channel walls.

Potentially similar processes occur on smaller scales as well and give rise to the entrapment of nanobubbles, too.

Finally, we would like to mention an interesting aspect of the experiment shown in Figures 4a and 6a. Because the channel is filled from both sides simultaneously, the air volume inside the channel is entrapped. As the two menisci approach each other, the air is progressively compressed and thereby builds up a counter pressure against the driving Laplace pressure. This leads to a slowing down and eventually to a complete stop of the menisci's motion. The only way for the gas to escape the nanochannel is to dissolve in the liquid, which is what we ultimately observe. Dimensional analysis suggests that the dynamics in this case should be diffusion limited: the characteristic convective time scale is given by  $\tau_{\text{conv}} = L\mu/\sigma_{\text{lv}} \approx O(0.01 \text{ s})$ , whereas the diffusive time scale is simple  $\tau_{\text{diff}} = L^2/D \approx O(1000 \text{ s})$  for a typical diffusivity of  $10^{-9} \text{ m}^2/\text{s}$ .

In conclusion, a nanofluidic chip was manufactured with an integrated Fabry–Pérot interferometer. By carefully optimizing the involved materials' parameters and fabrication procedures, a high finesse interferometer was obtained, which allowed for studying both the channel properties and the capillarity-driven dynamics of liquids inside the channels with high resolution. First test experiments revealed intriguing differences between ethanol and water filling with reduced filling speeds in the former and increased speeds in the latter case. Intensity profiles reflecting the refractive index of the medium inside the channel suggest the entrapment of air bubbles in the case of partially wetting water. We anticipate that the interferometric technique will allow for high accuracy measurements on the nanoscale dynamics in fluid–gas and fluid–fluid systems in future experiments.

**Acknowledgment.** K.v.D., D.M., J.E., and A.v.d.B. thank the Dutch Ministry of Economic Affairs for a Nanoned grant. H.R. and F.M. thank the German Science Foundation (DFG) priority program Nano and Microfluidics for financial support.

## References

- (1) Derjaguin, B. V.; Titiyevskova, A. S.; Abrikosova, I. I.; Malkina, A. D. *Discuss. Faraday Soc.* **1954**, *18*, 24–41. Sparnaaij, M. J. *Physica* **1958**, *24*, 751. Rouweler, G. C. J.; Overbeek, J. Th. G. *Trans. Faraday Soc.* **1971**, *67*, 2117.
- (2) Israelachvili, J. N.; Tabor, D. *Proc. R. Soc. London, Ser. A* **1972**, *331*, 19.
- (3) Tabor, D.; Winterton, R. H. S. *Proc. R. Soc. London, Ser. A* **1969**, *312*, 435.
- (4) Mugele, F.; Salmeron, M. *Phys. Rev. Lett.* **2000**, *84*, 5796. Becker, T.; Mugele, F. *Phys. Rev. Lett.* **2003**, *91*, 166104.
- (5) Israelachvili, J. *Intermolecular and Surface Forces*, 2nd ed.; Academic Press: New York, 1992.
- (6) Eijkel, J. C. T.; van den Berg, A. *Microfluidics Nanofluidics* **2005**, *1*, 249.
- (7) Wolffenbuttel, R. F. *J. Micromech. Microeng.* **2005**, *15*, S1452.
- (8) Waters, R. L.; Aklufi, M. E. *Appl. Phys. Lett.* **2002**, *81*, 3320.
- (9) Lin, C.-J.; Tseng, F.-G. *Sens. Actuators, A* **2004**, *113*, 12.
- (10) Heredero, R. L.; Santos, J. L.; Fernández de Caleyra, R.; Guerrero, H. *IEEE Sens. 2003* **2003**, *3*, 13.
- (11) Bondavalli, P.; Benyattou, T.; Garrigues, M.; Leclercq, J. L.; Jourba, S.; Pautet, C.; Hugon, X. *Sens. Actuators, A* **2001**, *94*, 136.
- (12) Calaza, C.; Fonseca, L.; Moreno, M.; Marco, S.; Cane, C.; Gracia, I. *Sens. Actuators, A* **2004**, *113*, 39.
- (13) Minas, G.; Martins, J. S.; Correia, J. H. *Sens. Mater.* **2002**, *14*, 77.
- (14) Christenson, G. L.; Tran, A. T. T. D.; Miller, S. A.; Haronian, D.; Lo, Y. H.; MacDonald, N. C. *Appl. Phys. Lett.* **1996**, *69*, 3324.
- (15) Sidorin, Y.; Blomberg, M.; Karioja, P. *IEEE Photonics Technol. Lett.* **1999**, *11*, 18.
- (16) Mijatovic, D.; Eijkel, J. C. T.; van den Berg, A. *Lab Chip* **2005**, *5*, 492.
- (17) Mao, P.; Han, J. *Lab Chip* **2005**, *5*, 837.
- (18) Haneveld, J. *Nanochannel Fabrication and Characterization Using Bond Micromachining*. Thesis. University of Twente, The Netherlands, 2006.
- (19) Han, A.; Mondin, G.; Hegelbach, N. G.; de Rooij, N. F.; Stauer, U. *J. Colloid Interface Sci.* **2006**, *293*, 151. Hibara, A.; Saito, T.; Kim, H.-B.; Tokeshi, M.; Ooi, T.; Nakao, M.; Kitamori, T. *Anal. Chem.* **2002**, *74*, 6170.
- (20) Tas, N. R.; Haneveld, J.; Jansen, H. V.; Elwenspoek, M.; van den Berg, A. *Appl. Phys. Lett.* **2004**, *85*, 3274.
- (21) Eijkel, J. C. T.; Dan, B.; Reemeijer, H. W.; Hermes, D. C.; Bomer, J. G.; van den Berg, A. *Phys. Rev. Lett.* **2005**, *95*, 256107.
- (22) Born, M.; Wolf, E.; *Principles of Optics*, 6th ed.; Cambridge University Press: Cambridge, 1999.
- (23) Heuberger, M. *Rev. Sci. Instrum.* **2001**, *72*, 1700.
- (24) Becker, T.; Mugele, F. *J. Phys.: Condens. Matter* **2005**, *17*, S319.
- (25) Hermes, D. C.; Heuser, T.; van der Wouden, E. J.; Gardeniers, J. G. E.; van den Berg, A. *Microsyst. Technol.* **2006**, *12*, 436.
- (26) See, e.g., deGennes, P. G.; Brochard, F.; Quéré, D. *Capillarity and Wetting Phenomena*; Springer: New York, 2004.
- (27) Tas, N. R.; Mela, P.; Kramer, T.; Berenschot, J. W.; van den Berg, A. *Nano Lett.* **2003**, *3*, 1537.
- (28) Geromichalos, D.; Mugele, F.; Herminghaus, S. *Phys. Rev. Lett.* **2002**, *89*, 169904.
- (29) Lefevre, B.; Saugey, A.; Barrat, J. L.; Bocquet, L.; Charlaix, E.; Gobin, P. F.; Vigier, G. *Colloids Surf. A* **2004**, *241*, 265.
- (30) For recent reviews, see: Lauga, E.; Brenner, M. P.; Stone, H. in *Handbook of Experimental Fluid Dynamics*; Foss, J., Tropea, C., Yarin, A., Eds.; Springer: New York, 2005, and Neto, C.; Evans, D. R.; Bonaccorso, E.; Butt, H.-J.; Craig, V. *Rep. Prog. Phys.* **2005**, *68*, 2859.

NL062447X